XAS study of Iron Oxide NPs for biomedical purposes

Report for Experiment HE 3602

1. Introduction

Magnetic nanoparticles (NPs) exhibit a reach variety of physical phenomena as monodomain regime, superparagnetism, or surface enhanced anisotropy that makes them interesting from a fundamental point of view [1] but also for several kind of applications as data storage [2], catalysis [3] or biomedical applications [4]. As concerns these later, iron oxide nanoparticles are preferred due to their high biocompatibility, in contrast with the very low one of most of other magnetic materials [5]. A key issue for the use of iron oxide nanoparticles in biomedical applications is to have monocrystalline and monodisperse nanoparticles with a very narrow size distribution [6,7,8]. As the magnetic properties at the nanoscale are strongly dependent on the particle size [9], a width size distribution rends almost impossible to reach the optimum performance simultaneously for most of the NPs. Grain boundaries in iron oxide NPs are known also to induce magnetic frustration weakening their saturation magnetization and magnetic performance [10,11]. Among the different methods for the synthesis of iron oxide nanoparticles, the seed-growth method [12] results particularly interesting since it provides high quality monocrystalline nanoparticles with a very narrow size distribution and a relative easy control of the particle size. However some recent studies has shown that these features (monocrystalline and narrow size distributions) are necessary conditions but not sufficient to exhibit good magnetic properties [13,14]

In a recent paper [14], we studied the synthesis and hyperthermia performance of iron oxide nanoparticles prepared with this seed-growth method. Despite the monocrystalline character of the NPs and their narrow size distribution the NPs resulted not useful for hyperthermia as their heating power was orders of magnitude lower than the expected one. A preliminary analysis of the magnetic properties of the NPs pointed out that the magnetic behavior was due to a poor magnetic shell structure as a consequence of the two pot synthesis method.

In this work we present a deeper and more systematic analysis of the magnetic properties of these NPs together with an study of their structure by means of X-ray absorption spectroscopy in order to correlate their magnetic behavior with the NPs structural features determined by the synthesis route.

2. Experimental

Synthesis..(Teresa)

The X-ray absorption measurements (X-ray Absorption Near-Edge Structure (XANES) and Extended X-ray Absorption Fine Structure (EXAFS)) were performed at the Fe K-edge energy at room temperature in conventional transmission mode using ionization chambers as detectors. The experiments were carried out at the BM25 Spanish CRG Beamline (SpLine) of the ESRF (European Synchrotron Radiation Facility). Each powder sample was sandwiched between two pieces of kapton tape located on the beam path. The amount of material was calculated to optimize the expected signal-to-noise ratio. Several scans were taken, in order to obtain a good signal-to-noise ratio. Fe metal foil was simultaneously measured for energy calibration. FeO, α-Fe_2O_3, γ-Fe_2O_3, and Fe_3O_4 powders were chosen as bulk references. Data analysis was carried out using *Athena* [15] program identifying the beginning of the absorption edge, E_0, the pre-edge and post-edge backgrounds. The spectra were subjected to a background subtraction and normalized by the edge jump. *Viper* [16] program was used process the normalized EXAFS signal as a function of the modulus of the photoelectron wavevector, k, $\chi(k)$ in the range of 2.5-12 Å^{-1}. The k^2 weighting was used to emphasize the signal at high energy of the spectrum. Previously, the signal was filtered by a Hanning window type and the phase and amplitude has been recalculated using FEFF code [17] version 6.01.

The magnetic characterization of the samples was carried out using Superconducting Quantum Interference Device (SQUID) from Quantum Design. Magnetization curves at low temperature (5 K) and the thermal dependence of the magnetization of liquid samples were recorded upon Zero Field Cooling (ZFC) and Field Cooling (FC). The concentration of iron oxide NPs in the liquid suspensions quantified by ICP-AES was used to normalize the magnetization values to the real content of iron oxide in the samples.

3. Results

3.1 Structural characterization

A Transmission Electron Microscopy (TEM) and X-ray diffraction (XRD) analysis of the NPs showed they were monocrystalline with a very narrow size distribution with uniform size that ranges from 6 to 18 nm as previously reported [14]. (include a TEM figure? A table with size and size dispersion?).
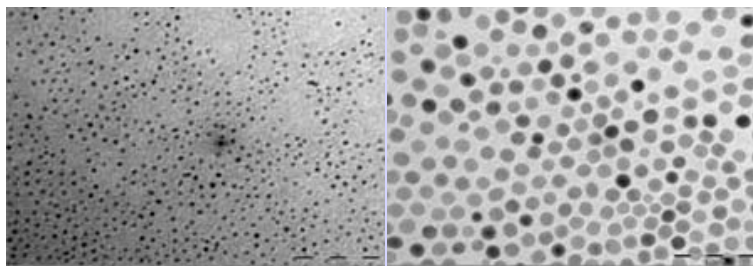

Fig.1 TEM image of iron oxide NPs transfer to water of (a) 6 nm and (b) 18 nm average particle size.

Comentario [M1]: Should we include TEM imge or a table with the sizes?

The diffraction peaks detected correspond to the standard pattern of a spinel structure. Within the magnetic iron oxides, magnetite (Fe_3O_4) and maghemite (γ-Fe_2O_3) present a similar inverse spinel structure with almost identical lattice parameters (8.385 Å and 8.346 Å for Fe_3O_4 and γ-Fe_2O_3 [18], respectively, although with different space groups, *Fd3m* and *P4$_3$32*). Therefore, distinguishing between both phases is considerable difficult with the above techniques.

However, magnetite contains a mixed valence of Fe^{2+} and Fe^{3+} with a ratio of $Fe^{2+}/Fe3+=\frac{1}{2}$ (with a average oxidation state of +2.67) while in maghemite is fully oxidized to Fe^{3+} with the presence of cation vacancies in octahedral positions to compensate the increased positive charge [18,19]. In both cases the Fe ions occupies both tetrahedral and octahedral sites. Hence, X-ray absorption spectroscopy techniques such as XANES and EXAFS at the Fe K-edge are powerful techniques to study the structure of the iron oxides [19,20,21,22]. XANES provides information of the oxidation state and EXAFS gives information about the local environment around the absorbing Fe ions including distances between atoms and coordination numbers of surrounding shells. This analysis can reveal the structure also in disordered and very small systems to account for the Fe short-range geometry and lead to the identification of crystal phases [23].

The XANES Fe K-edge measurements of the nanoparticles are presented in Figure 2. The XANES data for the bulk references (Fe foil, FeO, Fe_3O_4, α-Fe_2O_3 and γ-Fe_2O_3) are also shown for comparison. As at first observation, all samples have an average oxidation state similar to spinel references (Fig. 2(a)), confirming the results from the powder XRD measurement. However, both the white line (ffirst peak above the edge) and the second peak (7143 eV) resemble to magnetite reference. More precisely, considering the linear interdependence between energy edge shifts and the oxidation state of compounds of the same species, we can estimate the valence state of the samples [24] interpolating those from the references. The energy edge was taken from the first maximum of derivative spectra. The comparison of XAS derivatives allows appreciating possible subtle differences [25]: the shape of the derivative spectra reproduces quite well the transitions detected in magnetite. The calculated oxidation state of samples with sizes up to 10 nm is around +2.8 and, as the NPs size increases from that size, the absorption edge shifts to lower energies, with a +2.67, that is to Fe_3O_4 (Fig. 2(a)). A reduction of the oxidising state with increasing the particle size can be explained in terms of finite size effects: Magnetite NPs commonly exhibit an outer shell fully oxidised with Fe^{+3} ions. Smaller NPs present a larger fraction of surface atoms, and hence, a higher overall oxidation. However, in this case the oxidising state reduces progressively with the particle size, opposite to the behaviour observed in figure 2c , pointing out a qualitative change when the particles reach the 10 nm size.
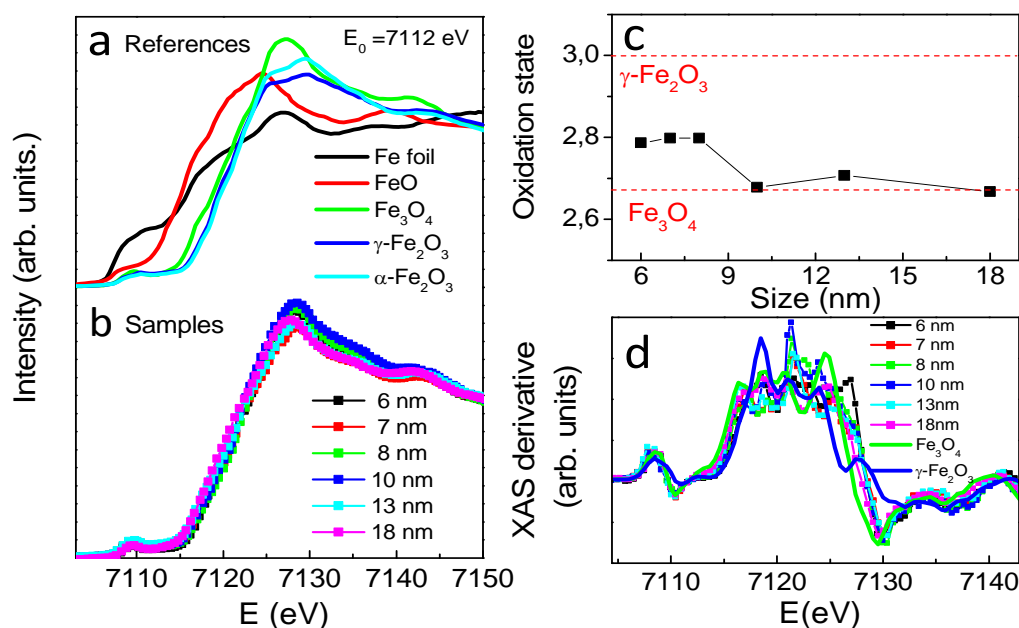
Figure 2. XANES spectra at the Fe K-edge of (a) the references (Fe metal, FeO, Fe_3O_4, γ-Fe_2O_3 and α-Fe_2O_3) and (b) of the NPs. (c) Estimated oxidation state of NPs. (d) Derivatives of NPs spectra compared to those of spinel references Fe_3O_4 and γ-Fe_2O_3.

The pseudo-radial distribution function around the Fe atom (Fig. 3) is obtained by performing Fourier Transform (FT) of the EXAFS signal weighted by k^2 in the range of k (2.70 to 12.16 Å^{-1}). The FT is related to the coordination spheres of atoms that absorb the radiation and its intensity is proportional of number of surrounded neighbours. It is relevant to note that the analysis of all samples, as well as references, was carried out under the same conditions, so that they are comparable.

The EXAFS signals $\chi(k)*k^2$ of the samples are almost identical to each other and they look again similar to magnetite (Fig. 3(a)). However, a very subtle diminishment around 5 Å^{-1} present in maghemite[19] can be also observed in the samples. Therefore, we can not rule out a fraction of maghemite in all the NPs although XANES analysis point outs a oxidation state close to magnetite, specially in larger NPs.

On the other hand, FT module as a function of distance of EXAFS signals (Fig. 3(b)) present two main peaks or average distances for both references and samples. The first peak corresponds to the radial distribution of oxygen with respect to iron (Fe-O distance) in either tetrahedral or octahedral sites [26]. The second peak is an average overlapping of the positions of the other iron atoms (Fe-Fe distance) between two octahedral sites, two octahedral sites and another tetrahedral site [27]. These average distances are characteristic of Fe_3O_4 and γ-Fe_2O_3 due to its similar spinel structure, although the differences in octahedral and tetrahedral of Fe positions may modify specially the shape of second peak. For example, the presence of cation vacancies in maghemite is reflected in a reduction the FT intensity corresponding to higher Fe-Fe distances.

We performed a fit of the experimental data with theoretical signals in the range of R of 0.8–3.8 Å. One oxygen shell was used to fit the first peak 1.96 Å for Fe-O bonds and three distances for the second for the different Fe-Fe bonds 2.50, 3.20 and 3.70 Å, respectively [27]. These values were initially adjusted considering Fe oxide references fixing the number of neighbours. This last analysis allowed to obtained the amplitude reduction factor S_o^2 to be used in the fit of NPs (S_o^2=0.6). Table II gives the obtained EXAFS parameters fitting results.
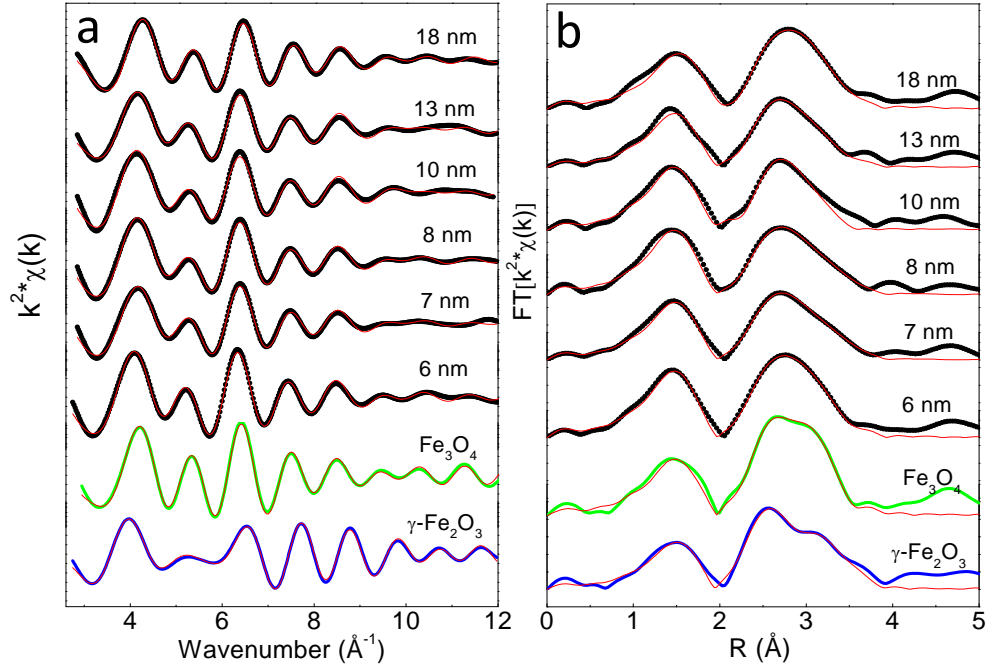

Figure 3. (a) EXAFS filtered signal, $\chi(k)*k^2$ and (b) Fourier transform function for the NPs and Fe_3O_4 and γ-Fe_2O_3 references.

Sample	Bond	R_j (Å)	N_j	σ_j (Å^{-1})
Fe_3O_4	Fe-O	1.97	3.73	0.006
	Fe-Fe	3.01	3.20	0.008
	Fe-Fe	3.50	6.40	0.008
	Fe-Fe	3.72	3.20	0.008
6 nm	Fe-O	1.94	3.20	0.008
	Fe-Fe	3.05	2.49	0.008
	Fe-Fe	3.53	1.69	0.010
	Fe-Fe	3.68	0.94	0.009
7 nm	Fe-O	1.94	3.22	0.008
	Fe-Fe	3.05	2.41	0.008
	Fe-Fe	3.53	1.84	0.010
	Fe-Fe	3.66	0.92	0.010
8 nm	Fe-O	1.94	3.21	0.007
	Fe-Fe	3.05	2.45	0.008
	Fe-Fe	3.52	1.99	0.010

	Fe-Fe	3.67	0.91	0.012
10 nm	Fe-O	1.94	3.20	0.009
	Fe-Fe	3.05	3.09	0.009
	Fe-Fe	3.51	2.38	0.010
	Fe-Fe	3.67	1.07	0.011
13 nm	Fe-O	1.95	3.17	0.009
	Fe-Fe	3.05	3.10	0.010
	Fe-Fe	3.52	2.40	0.012
	Fe-Fe	3.68	1.08	0.010
18 nm	Fe-O	1.94	3.17	0.008
	Fe-Fe	3.04	3.15	0.010
	Fe-Fe	3.51	2.42	0.011
	Fe-Fe	3.68	1.20	0.011

Table II. Fitting structural parameters of the coordination shell of reference Fe_3O_4 and nanoparticles at the Fe K edge. N is the coordination number (fixed for reference), Fe-O and Fe-Fe are the average interatomic distances and σ^2 are the Debye-Waller factors. The overall reduction factor S_0^2 was fixed to 0.6.

In general, a reduction of coordination of both shells has been detected in the NPs by the diminishment of the total number of neighbours, which it may be a consequence of the nanosize of the structure. This is especially noticeable in the decrease of the Fe-Fe relative intensity respect to Fe-O peak in comparison with spinel references. The radial distribution of distances is mostly centred around Fe_3O_4 values. The Fe-O bond fitted (1.94-1.95 Å) distance for the samples hardly varies with the diameter of nanoparticles and they are slightly lower than the corresponding to Fe_3O_4 reference. However, the Fe-O peak is slightly less intense for largest samples, which may be indicative of a presence of oxygen vacancies. The Fe-Fe fitted distances are quite similar between samples with slight variations. Since the EXAFS signals $\chi(k)*k^2$ do not seem to vary with the diameter of the particle, any subtle differences in the Fe-Fe distribution peak between samples can be due to different tetrahedral or octahedral sites occupation randomly distributed generating cation vacancies. Therefore, observing the EXAFS analysis, we can not detect a clear visible trend as the diameter of the NPs increases, concerning the occupation of Fe or O sites. This fact can be explained in terms of a complex migration of different vacancies that contributes to a broad distribution, specially in the Fe-Fe peak, but responsible of the change in the overall oxidation state observed in the XANES analysis.

Thus, the structural characterization of the samples points out a very similar structure without clear differences as a function of the particle size.

3.2 Magnetic properties

Figure 4 present the magnetization curves of the samples at 300 K and at 5 K upon FC and ZFC conditions. The magnetization was normalized to the iron oxide mass in the sample determined by ICP [14]. The curves measured at 5 K exhibit larger M_S values than those obtained at 300 K except for the largest NPs (~18 nm), for which Ms is almost identical at both temperatures. Moreover, for NPs smaller

than 10 nm the curves at 5 K are fully saturated upon field of 10 KOe while larger NPs exhibit a non-saturated component even at 50 KOe. The slope of this non-saturated component increases with the particle size.
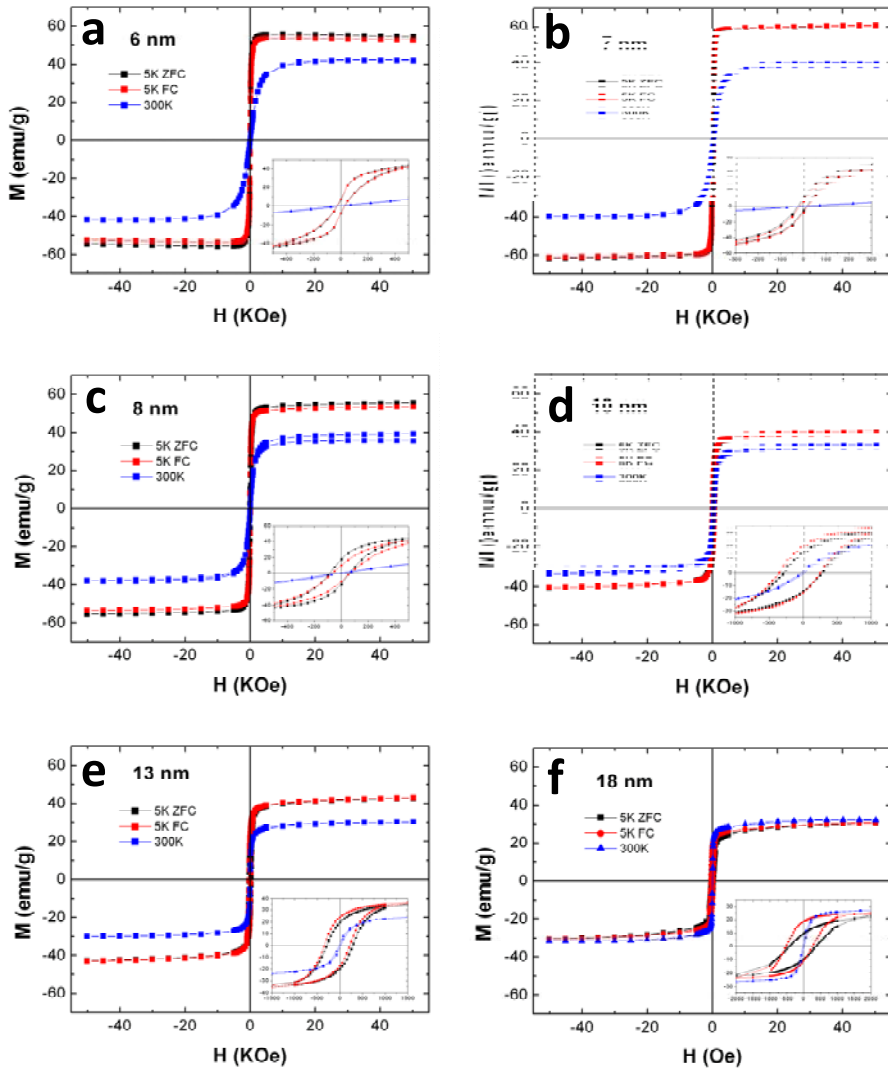

Figure 4. Magnetization curves at 300 K and at 5K upon FC ($H_{cooling}$=50 KOe) and ZFC. Insets show a detail of the low field region.

A numerical analysis of the curves provided the results summarized in figure 5. The saturation magnetization (M_S) values at 5 K are significantly smaller than those of bulk magnetite and maghemite (87 emu/g and 93 emu/g, respectively) [28]. For both 5 K and 300 K, the tendency is M_S to decrease with the particle size.
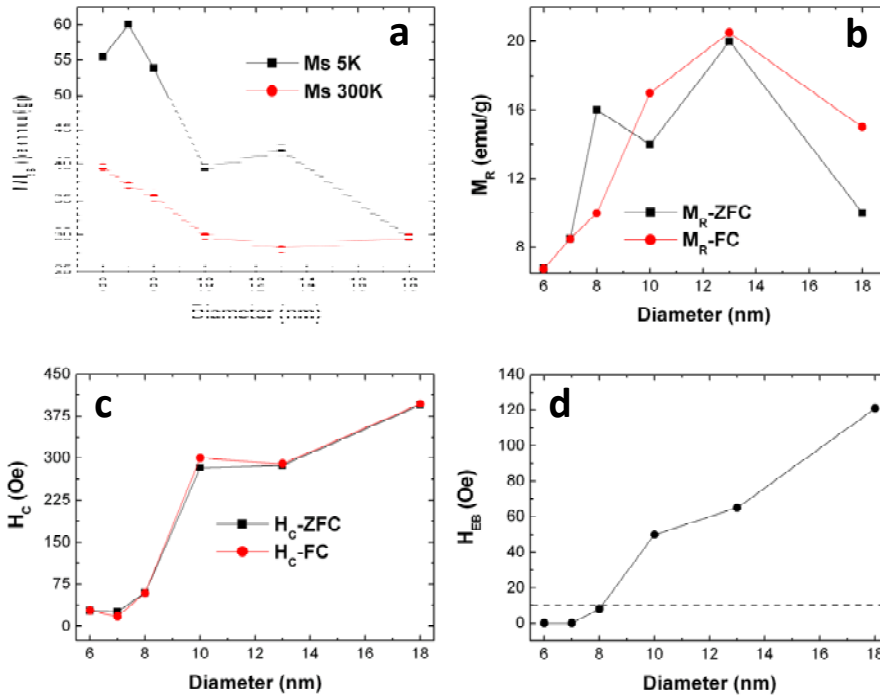
Figure 5. (a) Saturation Magnetization of the NPs at 5 K and 300 K (b) coercive field at 5 K and (c) exchange bias field at 5 K.

The remanence magnetization (M_R) at 5 K is below half of Ms, as it could be expected for a system composed of non-interacting NPs with a random distribution of anisotropy axis. The coercive field at low temperature (Fig. 5c) increases with the particle size (as expected for this size range) from 35 Oe for the 6 nm seeds to 400 Oe for the 18 nm NPs. There is clear jump in the tendency for the 10 nm size from which H_C exhibit a sharp increase. The initial 6 nm seeds and the 7 nm NPs does not exhibit any exchange bias. For 8 nm NPs there is a weak HEB (~8 Oe) while above 10 nm size the exchange bias field (H_{EB}) is noticeable and increases with the particle size as summarized in figure 5d.

The thermal dependence of the magnetization measured upon FC and ZFC conditions is presented in figure 6.
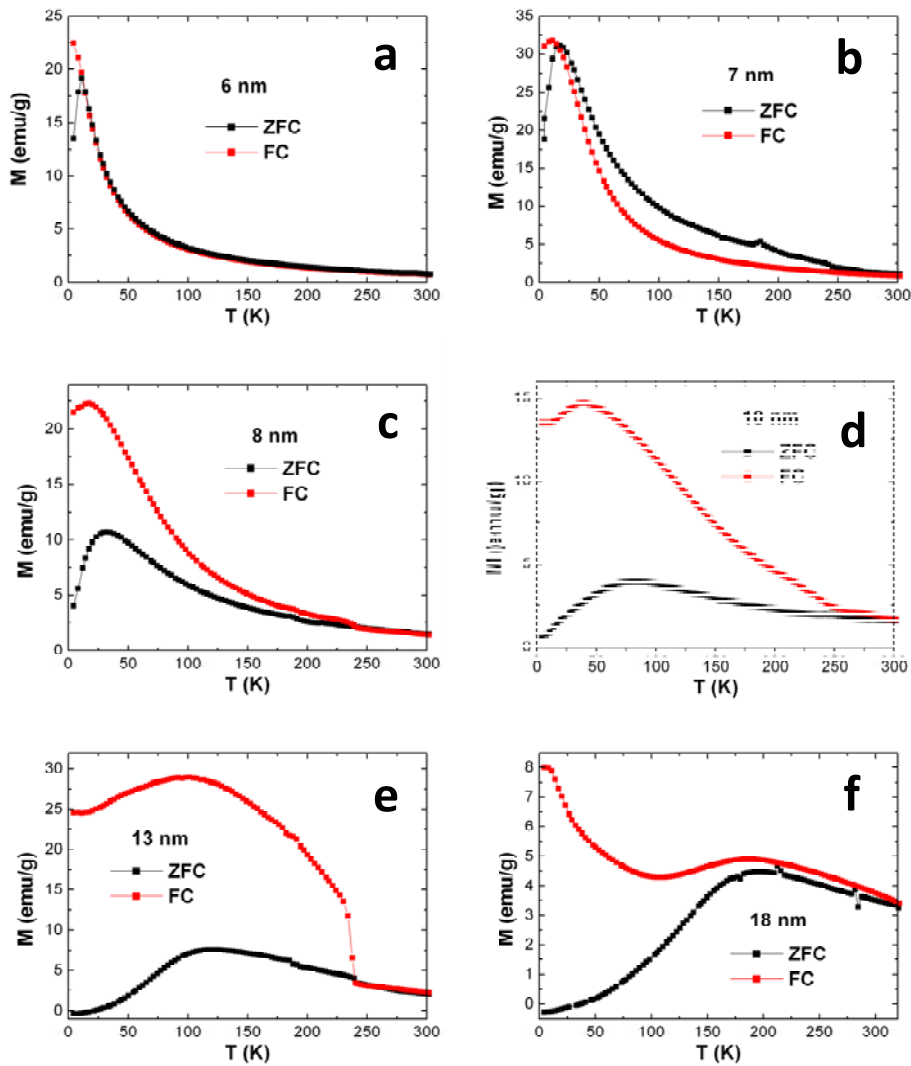
Figure 6. Thermal dependence of the magnetization for the nanoparticles applying a field of H_{meas}=100 Oe upon FC ($H_{cooling}$=50 KOe) and ZFC.

The curves present the typical profile of superparamagnetic nanoparticles with a well defined blocking temperature (TB). The curve obtained upon ZFC appears always below at obtained upon FC except for the case of 7 nm NPs for which they appear inverted above T_B. This behavior has been associated with antiferromagnetic correlations, spin frustration or irreversibility mechanisms.

A numerical analysis of these curves is presented in figure 7.
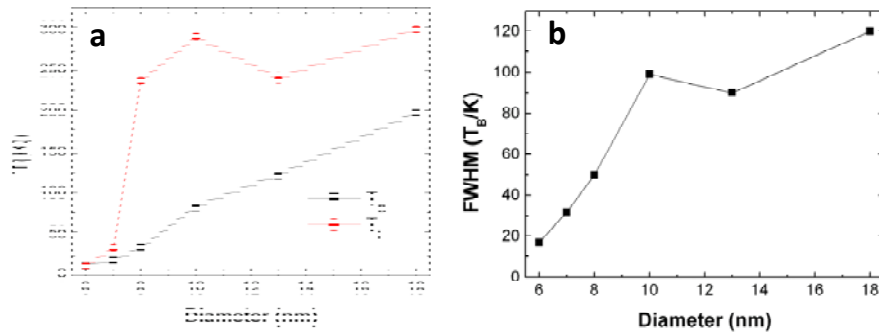
Comentario [M2]: Ask Mar

Figure 7. (a) Blocking temperature (T_B) and irreversibility temperature (T_IR) and (b) Full Width at Half Maximum (FWMH) of the ZFC curve as a function of the particle size

The blocking temperature (T_B) increases with the particle size exhibiting a deviation from the monotonic behavior for 10 nm size. The irreversibility temperature T_{IR} matches T_B for the initial seed, but not for larger NPs. As abovementioned, for the 7 nm NPs the FC and ZFC curves crosses so it is not obvious to define the T_{irr}. The crossover takes place below the TB suggesting..   For larger NPs the T_{IR} results significantly larger than T_B which is a fingerprint of intrparticle magnetic disorder and spin frustration.

Comentario [M3]: Ask Mar

The full width at half maximum (FWHM) of the ZFC curve as a function of the particle size is shown in figure 7b. The tendency is an increase of the FWHM with the particle size as expected. However, for the 10 nm NPs there is a clear deviation of the monotonic behavior with a sudden increase of the width, as it happens for the coercive field, exchange bias field and blocking temperature. This FWHM is associated with the distribution of energy barriers to overcome for spin inversion. Therefore the results summarized in figure 7 points out a significant variation of the anisotropy when the particles reach 10 nm size.

4. Discussion

The magnetic characterization of the NPs points out two remarkable features: the progressive reduction of M_S as the particle size increases and the qualitative change at 10 nm size where most of the magnetic parameters exhibit a singularity. This later was also observed in the oxidizing state measured from XANES spectra (figure 2). However, no clear differences were observed in the structural characterization carried out with EXAFS, XRD or TEM [14]. Therefore, the samples exhibit some magnetic disorder without structural disorder but related with their electronic configuration (the ultimate responsible of the magnetic behavior).

The initial seeds show very low M_S values, about 40 emu/g, which is less than half of the bulk material one. NPs usually exhibit reduced M_S values in comparison with bulk values due to size and surface

effects. These effect has been commonly accepted as unavoidable but recent works [29] showed that it is possible to reach M_S values very close to those of the bulk material (~90%) by using the appropriated preparation methods. Thus, the initial seeds exhibit some kind of magnetic disorder despite their excellent structural properties. This magnetic disorder is likely to be at the surface where the lack of symmetry favors the increase of oxygen and cation vacancies inducing magnetic frustration and consequently the formation of a shell with reduced magnetization [9,30,31,32,33,34,35]. Actually, the oxidizing state of the Fe cations obtained from XAS measurements is close to that of magnetite, with a possible fraction the maghemite, specially in smaller NPs. This suggests the existence of some oxygen and cation vacancies (electrically compensated by changes in the Fe oxidising state) that accounts for the reduced magnetization layer.

However, the M_S values for the larger NPs grown on these seeds can not be ascribed to these surface effects. In this case M_S should increase with the particle size since this shell represent a smaller fraction of the whole NPs as the size increases, while we observe here the opposite trend. Because of the reduced M_S value of the initial seed, the shell grows on a magnetically poor surface yielding to a magnetic layer also with some magnetic frustration and reduced M_S. This layer represents a higher fraction of the particle as the size increases and consequently the M_S decreases for larger NPs. Luigjes et al. prepared monocrystalline iron oxide particles following the same synthesis method [12] and for a size larger than 10 nm, their ferromagnetic diameters were also smaller than expected from TEM, presenting magnetic polidispersity. They could correlate they presence of defects in the intial seeds with a deterioration of the magnetic properties. It turns out that the layer grown on these seed will exhibit poor magnetic properties and reduced magnetization Therefore, to obtain magnetic nanoparticles with high magnetization values using a seed-growth method it is essential to ensure an excellent crystal quality of the initial seeds

The other key feature of the NPs is the observed qualitative change for the 10 nm size. The sudden increase in the coercive field and blocking temperature for the 10 nm NPs suggest this is not due to size effects but to the development of an additional source of anisotropy for this size. The anisotropy constant can be determined from the thermal dependence of the magnetization upon ZFC according to:

$$K_u = 25 \frac{k_B T}{V}$$
(1)

being V the nanoparticle volume and K_B the Boltzman constant. The anisotropy can be also calculated from the coercive field at low T according to:

$$H_C = \alpha \frac{2K_u}{M_S} \left(1 - \left(\frac{T}{T_B} \right)^{\frac{1}{2}} \right)$$
(2)

Where α is a parameter that for the case of NPs with a random distribution of anisotropy axis is 0.48.

We calculated the anisotropy using both equations for the different particle sizes. Results are presented in figure 8. The anisotropy constant was determined according to equation (1) using both the real volume of the particles obtained from the TEM analysis and also the effective magnetic volume: since the magnetization of the particles is smaller than the bulk one, we assume that just a fraction of the particle volume is ferromagnetic. This magnetic volume is obtained multiplying the TEM volume by the experimental Ms of the particles and dividing by the saturation magnetization of bulk magnetite (90 emu/g). Similarly the calculation of the anisotropy with equation 2 was performed using the experimental value of M_S and that of the bulk $M_{S\text{-}bulk}$. This later also makes sense: The nanoparticle has a magnetically frustrated layer and a ferromagnetic core. This core is the main responsible of the magnetic properties and it will have a saturation magnetization close to the bulk one
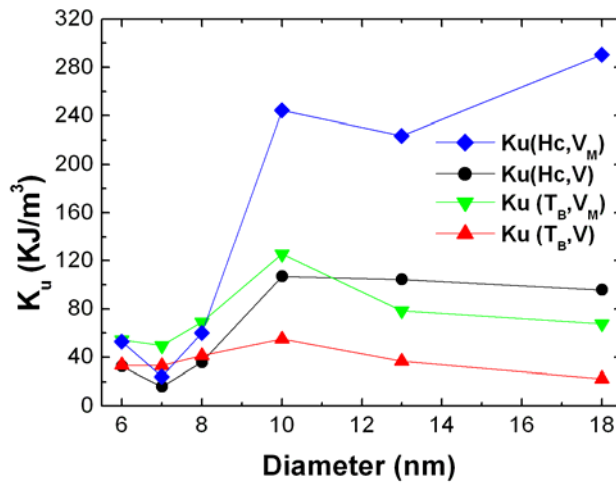

Figure 8. Uniaxial anisotropy constant for the nanoparticles obtained from the values of Hc (eq. 1) and from the blocking temperature (eq. 2). In the first case the calculation was carried out using the NPs volume obtained from TEM (H_C, V_{TEM}) and the magnetic volume determined from the experimental M_S (H_C, V_{MAG}) as described in the text. For the second, calculation was performed using the experimental M_S value (TB, $M_{S\text{-}exp}$) and the Ms bulk one for magnetite (TB, $M_{S\text{-}bulk}$)

While it is tough to determine which is the best method to calculate the anisotropy, there are some common trends in the size dependence of the anisotropy constant K. Initially, the anisotropy decreases with the particle size but there is a sudden increase when reaching the 10 nm size. Actually this increase stars already for the 8nm NPs. The K values for the initial seeds are in the range 35 to 55 KJ·m^{-3} depending on the calculation method. These values are higher than the anisotropy constant for bulk magnetite (18 KJ/m3) or maghemite (20 KJ/m3). It is well reported for iron oxide nanoparticles that the lack of symmetry at the surface increases the anisotropy leading to a surface shell with enhanced anisotropy (surface anisotropy) [30]. The surface is a preferential site for vacants migration that induces magnetic frustration, spin canting and spin glasses. As the particle size increases this shell represent a

smaller fraction of the whole nanoparticle volume so the effective anisotropy decreases towards the volume value. However, the sudden increase of anisotropy observed when reaching the 10 nm size can not be explained by this surface effect. This trend is observed also for all the calculations method pointing out some kind of qualitative change for this size. The fact that the sudden increase of anisotropy is not observed in all the nanoparticles with a grown layer but when they reach a certain size suggests that this phenomenon is not intrinsic of the layers but related to their growing process.

The increase of anisotropy coincides with the onset of the exchange bias (figure 5d) a phenomenon that takes place when two magnetic phases with different features becomes in contact [36,37,38]. Actually, exchange bias has been also observed when phases with same composition if the interface shows some kind of magnetic disorder [39]. These interfaces can not correspond to the seed-growing layer one. In this case, the exchange bias should be observed already for all the NPs with a grown layer, in particular for the 8 nm NPs (2 nm thicknesses is enough to observe exchange bias).

Antiphase boundaries (APB) are a well known magnetic defect that does not require structural defects. APB are been extensively observed and studied in magnetite films epitaxially grown on MgO [40,41,42,43]. Within the seed-growth method, islands of magnetite epitaxially grow over the initial seed facets until they percolate forming a continuously film. Our "substrate" is not flat be rounded, inducing slight mismatches at the edges were the island percolate favoring the formation of APB (in the case of MgO substrates the difference in lattice parameter induces the mismatch). The presence of these antiphase boundaries in the magnetite film grown over MgO also arise exchange bias as that observed here. Moreover, the magnetization curves al low Temperature upon FC and ZFC exhibit a very similar shape to that we found here (see figure 4f and figure 2 in reference [40]). Hence, we conclude that the origin anisotropy enhancement is the appearance of APB when the layers grown over the initial seeds.

This phenomenology may be partially responsible of the reduction of M_S with the particle size. However, the fact that Ms decreases progressively while the increase of anisotropy takes place abruptly at a certain size suggests they are different phenomena.

The evolution of anisotropy with the particle size turns out that the nanoparticles exhibit a kind of magnetic memory. Their magnetic properties resemble the fact that they were grown in two steps so they behave as a complex system despite they are monocrystalline. Such a memory could be erased by heating over their order temperature (850ºC), but this process is not possible since the nanoparticles would aggregate and grow. Consequently, there is no chance to delete the magnetic complexity of the nanoparticles, suggesting that two pot methods are not suitable to obtain iron oxide nanoparticles with for biomedical applications.

5. Conclusions

In summary, we found here that iron oxide nanoparticles prepared using a two-pot synthesis does not seems to be suitable for biomedical applications. There are two issues that account for the deterioration of the magnetic properties. On the one hand the presence of defects in the initial seeds induces a shell with high concentration of defects and consequently reduced magnetization. The layers growing on these bad magnetic shell exhibit also poor magnetic properties yielding to a progressive decrease of the saturation magnetization when increasing the particle size. This problem can be overcome by using seeds with excellent crystal quality as recently demonstrated [29]. On the other hand, when the islands nucleated on the initial seeds surfaces percolate they form antiphase boundaries that increase the anisotropy and induce magnetic frustration. Consequently the system exhibits qualitative changes in the magnetic properties for this critical size (~10 nm). Despite the monocrystalline and monodisperse character of the NPs, they retain a kind of magnetic memory that resembles the fact that they were grown in two steps and are composed of an initial seed plus and additional layer subsequently grown that increases with the NP size. There is not an evident solution for this issue, pointing out that two-pot methods are not suitable for the fabrication of small iron oxide nanoparticles for biomedical applications despite the fact that they exhibit excellent structural properties.

References

1 A. H. Lu, E. L. Salabas, F. Schuth. Angew. Chem., Int. Ed. 46, 1222 (2007)

2 S. H. Sun, C. B. Murray, D. Weller, L. Folks, A. Moser. Science 287, 1989 (2000).

3 A.H. Lu, W. Schmidt, N. Matoussevitch, H. BPnnermann, B. Spliethoff, B. Tesche, E. Bill, W. Kiefer, F. SchVth, Angew. Chem. 116, 4403 (2004).

4 Q. A. Pankhurst, J. Connolly, S. K. Jones, J. Dobson. J. Phys. D: Appl. Phys. 36, R167 (2003).

5 A. K. Gupta, M. Gupta. Biomaterials 26, 3995 (2005).

6 A. Figuerola, R. Di Corato, L. Manna, T. Pellegrino. Pharmacological Research 62, 126 (2010).

7 J.P. Fortin, C. Wilhelm, J. Servais, C. Menager, J. C. Bacri and F. Gazeau, J. Am. Chem. Soc. 129, 2618 (2007)

8 P. Poddar, T. Fried and G. Markovich, Phys. Rev. B 65, 172405 (2002).

9 X. Batlle, A. Labarta. J. Phys. D: Appl. Phys. 35, R15 (2002).

10 J. M. D. Coey Phys. Rev. Lett. 27 1140 (1971).

11 T. N. Shendruk, R. D. Desautels, B. W. Southern, and J. van Lierop, Nanotechnology 18, 455704 (2007)

12 S. Sun, H. Zeng. J. Am. Chem. Soc. 124, 8204 (2002).

13 B. Luigjes, S. M. C. Woudenberg, R. de Groot, J. D. Meeldijk, H. M. Torres Galvis, K. P. de Jong, A. P. Philipse, and B. H. Erné. J. Phys. Chem. C 115, 14598 (2011)

14 M. Levy, A. Quarta, A. Espinosa, A. Figuerola, C. Wilhelm, M. Garcia-Hernandez, A. Genovese, A. Falqui, D. Alloyeau, R. Buonsanti, P. D. Cozzoli, M. A. Garcia, F. Gazeau and T. Pellegrino. Chem. Mat. 23, 4170 (2011).

15 M. Newville, J. Synchrotron Radiat. 8, 322 (2001).

16 K.V. Klementev, J. Phys. D: Appl. Phys. 34, 209 (2001).

17 J. J. Rehr, Jpn.J.Appl.Phys. 32, 8 (1993).

18 C. Wang, D.R. Baer, J.E. Amonette, M.H. Engelhard, J. Antony, and Y. Qiang, J. Am. Chem. Soc. 131, 8824-32 (2009).

19 A. Corrias, G. Mountjoy, D. Loche, V. Puntes, A. Falqui, M. Zanella, W.J. Parak, and M.F. Casula, J. Phys. Chem. C 113, 18667-18675 (2009).

20 A. Corrias, G. Ennas, G. Mountjoyb, G. Paschinaa. Phys. Chem. Chem. Phys. 2, 1045 (2000).

21 A. Espinosa, A. Serrano, A. Llavona, J. Jimenez de la Morena, M. Abuin, A. Figuerola, T. Pellegrino, J. F. Fernández, M. Garcia-Hernandez, G.R. Castro, and M. A. Garcia, Meas. Sci. and Tech. 23, 015602 (2012).

22 F. Jiao, J.-C. Jumas, M. Womes, A.V. Chadwick, A. Harrison, and P.G. Bruce, J. Am. Chem. Soc. 128, 12905 (2006).

23 F. Jiménez-Villacorta, J. Sánchez-Marcos, E. Céspedes, M. García-Hernández, and C. Prieto, Phys. Rev. B, 82, 1 (2010).

24 V. Kunzl. Collect. Trav. Chim. Tchecolovaquie 4, 213 (1932).

25 A. Cabot, V.F. Puntes, E. Shevchenko, Y. Yin, Ll. Balcells, M. A. Markus, S. M. Hughes, A.. Paul Alivisatos1 (supporting information). J. Am. Chem. Soc. 129, 10358-10360 (2007).

26 L. Signorini, L. Pasquini, L. Savini, R. Carboni, F. Boscherini, E. Bonetti, A. Giglia, M. Pedio, N. Mahne and S. Nannarone Phys. Rev. B 68, 195423 (2003).

27 D. Carta, M.F. Casula, G. Mountjoy, and A. Corrias, Phys. Chem. Chem. Phys.10, 3108 (2008).

28 B. D. Culliti and C. D. Graham. Introduction to Magnetic Materials. IEEE Press, WILEY. Second Edition (2009).

29 X: Batlle et al J. Appl. Phys. 109, 07B524 (2011)

30 Shendruk, T. N.; Desautels, R. D.; Southern, B. W.; van Lierop, J. Nanotechnology 2007, 18, 455704

31 Pellegrino, T.; Manna, L.; Kudera, S.; Liedl, T.; Koktysh, D.; Rogach, A. L.; Keller, S.; R€adler, J.; Natile, G.; Parak, W. J. Nano Lett.

2004, 4, 703.

32 Guardia, P.; Batlle-Brugal, B.; Roca, A. G.; Iglesias, O.; Morales, M. P.; Serna, C. J.; Labarta, A.; atlle, X. J. Magn. Magn. Mater. 2007, 316, e756.

33 Pankhurst, Q. A.; Pollard, R. J. Phys. Rev. Lett. 1991, 67, 248.

34 Morales, M. P.; Veintemillas-Verdaguer, S.; Montero, M. I.; Serna, C. J.; Roig, A. Casas, L.; Martinez, B.; Sandiumenge, F. Chem. Mater. 1999, 11, 3058.

35 Linderoth, S.; Hendriksen, P. V.; Bodker, F.; Wells, S.; Davies, K.; Charles, S. W.; Morup, S. J. Appl. Phys. 1994, 75, 6583.

36 Meiklejohn, W. H.; Bean, C. P Phys. Rev. 105, 904–913 (1957)

37 Nogues, J.; Schuller, I. K. J. Magn. Magn. Mater. 1999, 192, 203.

38 Nogues, J.; Sort, J.; Langlais, V.; Skumryev, V.; Surinach, S.; Munoz, J. S.; Baro, M. D. Phys. Rep. 2005, 422, 65.

39 B. Martınez, X. Obradors,1 Ll. Balcells, A. Rouanet, and C. Monty, Phys. Rev. Lett. 80 (1998) 181

40 Arora, S. K.; Sofin, R. G. S.; Nolan, A.; Shvets, I. V. J. Magn. Magn. Mater. 2005, 286, 463.

41 Novakova, A. A.; Lanchinskaya, V. Y.; Volkov, A. V.; Gendler, T. S.; Kiseleva, T. Y.; Moskvina, M. A.; Zezin, S. B. J. Magn. Magn. Mater. 2003, 258, 354.

42 Margulies, D. T.; Parker, F. T.; Rudee, M. L.; Spada, F. E.; Chapman, J. N.; Aitchison, P. R.; erkowitz, A. E. Phys. Rev. Lett. 1997, 79, 5162.

43 W. Eerenstein, Phys Rev. B 68, 014428 (2003)